



# Magnetic and dielectric studies of barium hexaferrite ( $\text{BaFe}_{12}\text{O}_{19}$ ) ceramic synthesized by chemical route

Atendra Kumar<sup>1</sup> · Shiva Sundar Yadava<sup>1</sup> · Pooja Gautam<sup>1</sup> · Ankur Khare<sup>1</sup> · K. D. Mandal<sup>1</sup>

Received: 28 April 2017 / Accepted: 28 May 2018 / Published online: 28 June 2018  
© Springer Science+Business Media, LLC, part of Springer Nature 2018

## Abstract

Barium hexaferrite  $\text{BaFe}_{12}\text{O}_{19}$  (BHF) ceramic was synthesized by chemical route on sintering at 1050 °C for 12 h. The synthesized material was characterized by XRD, SEM, AFM and TEM analysis. Metal oxide stretching frequencies corresponding to Fe-O, Ba-O, and Fe-O-Fe bands are confirmed by FTIR studies. The hexagonal nature of the BHF ceramic was confirmed by TEM analysis and Rietveld refinement with space group  $P6_3/mmc$ . The particle size observed by TEM is 175 nm. The root means square and average roughness were found to be 61.048 nm and 44.025 nm respectively. The M-T and M-H hysteresis loop indicates temperature dependent ferromagnetic behavior of BHF ceramic. The temperature and frequency dependent dielectric properties were explained by Maxwell-Wagner theory. The value of dielectric constant ( $\epsilon'$ ) for BHF ceramic was found to be  $22 \times 10^3$  at 100 Hz and 483 K.

**Keywords** Chemical route · Rietveld refinement · Dielectric properties · Magnetic behavior

## 1 Introduction

Ferromagnetic Oxides (ferrites) were firstly introduced in 1952 and dominated gradually in the field of the permanent magnet. Depending on the crystal structure and chemical formula, hexaferrites are divided into five categories such as W-type ( $\text{BaMe}_2\text{Fe}_{16}\text{O}_{27}$ ), X-type ( $\text{Ba}_2\text{Me}_2\text{Fe}_{28}\text{O}_{46}$ ), Y-type ( $\text{Ba}_2\text{Me}_2\text{Fe}_{12}\text{O}_{22}$ ), Z-type ( $\text{Ba}_3\text{Me}_2\text{Fe}_{24}\text{O}_{41}$ ) and M-type barium hexaferrite,  $\text{BaFe}_{12}\text{O}_{19}$  (BHF). It exists in different form such as garnets, cubic, hexagonal, orthoferrites. M-type barium hexaferrite acquires an important class of magnetic material due to their electrical and magnetic properties with excellent chemical stability and low-cost production [1–3]. Ceramic industry requires the materials having high magneto-crystalline anisotropy, high saturation magnetization, high Curie temperature, high coercivity, the high natural resonant frequency with an excellent capability and corrosion resistance [4–6]. In addition to this, because of intrinsic magneto-crystalline anisotropy field in BHF ceramic, it can be used at much higher frequency than the ferrites with spinel and garnet structure [7].

Barium hexaferrite ( $\text{BaFe}_{12}\text{O}_{19}$ ) meets these properties very well, and it becomes one of the most high-tech materials in recent years [8]. The hexagonal structure of BHF ceramic is an M-type hexaferrite. The synthesis of M-type hexaferrites by several methods such as citrate precursor, hydrothermal, micro-emulsion, glass crystallization, sol-gel, sonochemical, co-precipitation, Nonconventional methods and mechanochemical activation were reported earlier [9–17]. Although ferroelectricity and ferromagnetism rarely coexist in these materials [18], mostly afford weak ferromagnetism because at room temperature, multiferroism is essential to understanding for multiferroic devices that exhibits coupling between ferroelectric and ferromagnetic order at ambient condition. M-type hexaferrite has great attentions due to its simplest crystalline structure among hexagonal ferrite and ferromagnetism at room temperature due to the presence of an unpaired electron in d-orbital of iron. It was widely used in various applications like computer data storage, video recorder and disk driver, high-density perpendicular magnetic and magneto-optic recording media [19, 20]. The electrical properties of the materials as a function of temperature (isothermal), time (isochronal) and frequency are usually referred as regarding dielectric constant, which are important properties of ferrite. The electrical property measurements related to the dielectric loss over a frequency range of 1 MHz–1 GHz. The dielectric constant and loss characteristics of the material are necessary for fabricating electrical and

✉ K. D. Mandal  
kdmandal.apc@itbhu.ac.in

<sup>1</sup> Department of Chemistry, Indian Institute of Technology (Banaras Hindu University), Varanasi, Uttar Pradesh 221005, India

electronic devices [21]. In the present Work, BHF ceramic was synthesized by the chemical method for the improvement of dielectric constant and dielectric loss, microstructural and magnetic properties of the materials.

## 2 Experimental

### 2.1 Material synthesis

Barium hexaferrite was synthesized by chemical route. The starting materials were taken as barium nitrate  $\text{Ba}(\text{NO}_3)_2$  (99% Merck, India), iron nitrate  $\text{Fe}(\text{NO}_3)_3 \cdot 9\text{H}_2\text{O}$  (98% Merck, India), and citric acid  $\text{C}_6\text{H}_8\text{O}_7 \cdot \text{H}_2\text{O}$  (99% Merck, India). The stoichiometric amount of  $\text{Ba}^{+2}$  and  $\text{Fe}^{+3}$  ions were dissolved in distilled water and per equivalent to metal ions of citric acid was added to this reaction mixture. The obtained reaction mixture was heated on hot plate with continuous stirring at 70–80 °C to evaporate water. After removal of water, a fluffy mass obtained which was burn with sooty flame at higher temperature. The resulting ash was ground with the help of agate and mortar to make fine powder. The powder was calcined at 850 °C for 8 h. Calcined powder was used to make cylindrical pellets (13 mm  $\times$  1.6 mm) with the help of PVA binder on applying 4 tons of pressure for 60 Second. These pellets were sintered at 1050 °C for 12 h and further used for characterization, dielectric and magnetic measurements.

### 2.2 Characterization

The diffraction pattern of sintered BHF ceramic was recorded by X-ray diffractometer (Rigaku miniflex 600, Japan) using  $\text{Cu-K}\alpha$  radiation ( $\lambda = 1.54 \text{ \AA}$ ) with scan rate of 2°/min. The FTIR spectra of sintered powder was characterized by ATR-FTIR (Bruker, ALPHA model) Spectrophotometer using KBr pellets in the frequency range 500–1500  $\text{cm}^{-1}$ . The surface morphology was observed by scanning electron microscope (ZEISS model, EVO18 Germany) whereas elemental composition was analyzed by EDX (Oxford instrument; USA). The particle size was examined by transmission electron microscope (TEM TECHNAI G<sup>2</sup> 20 TWIN). For TEM measurement the small amount of sample was dispersed in acetone and sonicated for 30 min. A drop of this solution was put on a carbon-coated copper grid and dried in hot air oven for 1 h. Magnetic measurements were carried out with a Quantum Design MPMS-3, over a temperature range 5–300 K and applied a magnetic field of  $\pm 2$  T. In addition to this, temperature dependent Zero field cooling (ZFC) and field cooling (FC) magnetization were also recorded at 100 Oe applied field using SQUID VSM dc magnetometer in the same temperature range. Silver-coated cylindrical pellets were

used for dielectric measurement by LCR meter (PSM 1735, NumetriQN4L U.K.).

## 3 Results and discussion

Single-phase formation of  $\text{BaFe}_{12}\text{O}_{19}$  ceramic sintered at 1050 °C for 12 h is confirmed from XRD pattern shown in Fig. 1(a), all diffraction peaks are index with JCPDS file (27–1029). The diffraction pattern of BHF ceramic sintered at 900 °C for 12 h shown in Fig. 1(b), indicates minor impurity of  $\alpha\text{-Fe}_2\text{O}_3$  with JCPDS file (89–7074) which vanished at 1050 °C for 12 h support single-phase formation. Rietveld refinement data of BHF ceramic showing hexagonal cell with space group  $\text{P6}_3/\text{mmc}$  shown in Fig. 2. The lattice parameters are given in Table 1 and observed cell ratio  $c/a$  is found to be 3.9399 that has been reported earlier [22]. Rietveld refinement parameters and atomic positions are shown in Table 2. It is observed from the Table that the oxidation state of Fe is +3 only, which is occupied five different planes of the hexagonal unit cell. The average crystallite size was calculated by taking the most intense peaks of BHF ceramic using the Debye-Scherrer formula.

$$D = k\lambda/\beta \cos\theta \quad (1)$$

where  $k$  is the shape coefficient value taken as 0.90,  $\lambda$  is the wavelength of X-ray,  $\theta$  is the diffraction angle, and  $\beta$  is the peak width of the diffraction peak at half-maxima (FWHM) in radians. The  $\beta$  is corrected value of diffraction peak due to instrumental broadening for crystallite size with reference to standard silicon wafer sample. The average crystallite size of BHF ceramic is found to be 59.83 nm. Figure 3 shows the FTIR spectra of the BHF ceramic sintered at 1050 °C for 12 h,

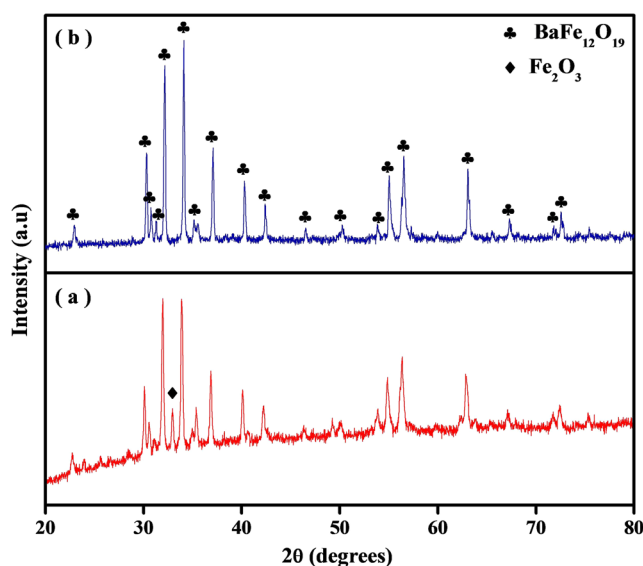
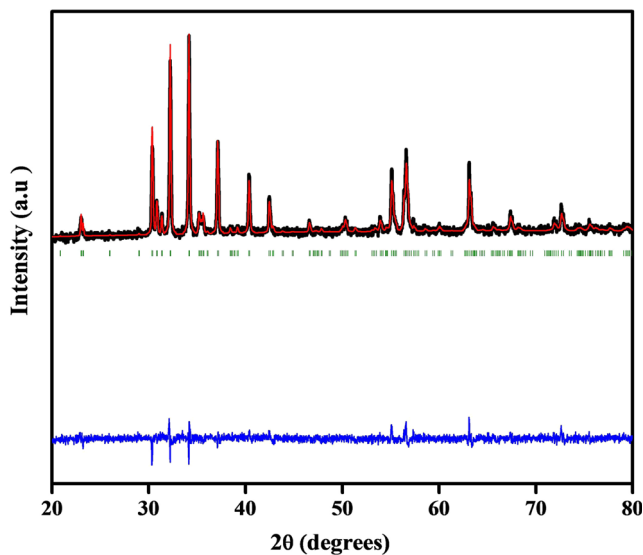


Fig. 1 (a) and (b) shows XRD diffraction patterns of BHF ceramic sintered at 900 °C and 1050 °C respectively for 12 h



**Fig. 2** Experimentally observed (black line), Rietveld calculated (red line) and their difference (blue bottom line) profile obtained after Rietveld analysis of XRD data for BHF ceramic using hexagonal structure in the space group  $P6_3/mmc$ . The vertical tick marks above the bottom line show peak position

recorded in the frequency range  $500\text{--}1500\text{ cm}^{-1}$ . Two absorption peaks at  $540$  and  $575\text{ cm}^{-1}$  represents Fe-O stretching vibration bands corresponding to octahedral and tetrahedral sites in the BHF ceramic. The Ba-O bands also present at  $895\text{ cm}^{-1}$  and Fe-O-Fe bands observed in between  $1100$  and  $1500\text{ cm}^{-1}$  which gives the qualitative information about metal oxide bonds of the BHF ceramic [23].

The bright field TEM image of the  $\text{BaFe}_{12}\text{O}_{19}$  ceramic sintered at  $1050\text{ }^\circ\text{C}$  for 12 h is shown in Fig. 4(a, b). TEM graphic revealed that the ultrafine powder is the crystalline in nature. The particles size of hexagonal BHF ceramic is equal to  $175\text{ nm}$ , which is greater than the crystallite size. The particles are formed with the combination of few crystallites due to which the particle size is larger than the crystallite size. High-resolution imaging by TEM is shown in Fig. 4(c), emerges the corresponding planes of BHF ceramic having inter-planer spacing  $d = 2.74, 2.90$  and  $4.66\text{ \AA}$  with  $(1\ 0\ 7)$ ,  $(0\ 0\ 8)$  and  $(1\ 0\ 2)$  planes respectively. The selected area diffraction (SAED) pattern of the ceramic shows bright spot patterns indicates corresponding planes  $(3\ 0\ 0)$ ,  $(1\ 1\ 6)$  and  $(1\ 0\ 4)$  which mentioned in Fig. 4(d). The zone axis of the diffraction pattern between  $(3\ 0\ 0)$  and  $(1\ 0\ 4)$  plane is found to be  $[0\ \bar{1}\ 2\ 0]$ . All the planes obtained from HR-TEM and SAED

**Table 1** Cell parameters for barium hexaferrite ( $\text{BaFe}_{12}\text{O}_{19}$ ) ceramic

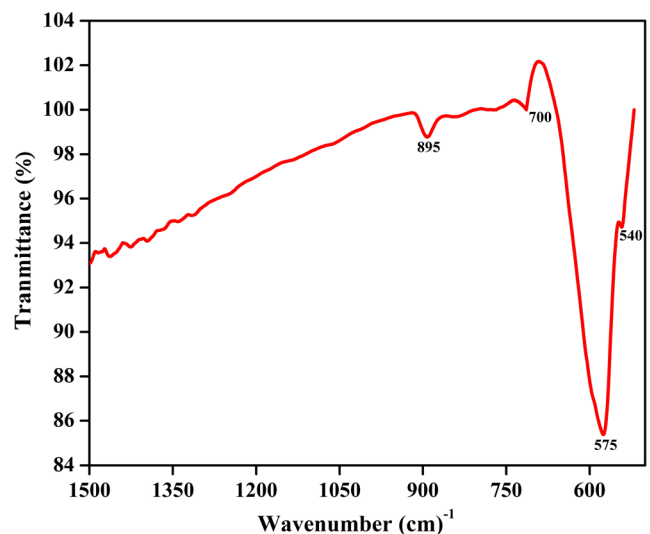
Cell parameters	$a = b = 5.88603\text{ \AA}$	$c = 23.18299$
Cell ratio	$c/a = 3.9399$	–
Angle	$\alpha = \beta = 90.0000^\circ$	$\gamma = 120.0000^\circ$
Cell Volume	$695.5767\text{ \AA}^3$	–

**Table 2** Refined structural parameters of  $\text{BaFe}_{12}\text{O}_{19}$  with Space Group  $P6_3/mmc$  (194), Bragg R-factor: 2.19, RF factor: 2.54,  $\chi^2$ : 1.16

Atom	Ox	X	Y	Z
Ba	+2	0.66667	0.33333	0.25000
Fe 1	+3	0.00000	0.00000	0.00000
Fe 2	+3	0.00000	0.00000	0.26100
Fe 3	+3	0.33333	0.66667	0.02700
Fe 4	+3	0.33333	0.66667	0.19010
Fe 5	+3	0.17000	0.34000	0.10850
O 1	–2	0.00000	0.00000	0.14400
O 2	–2	0.33333	0.66667	0.05500
O 3	–2	0.18600	0.37300	0.25000
O 4	–2	0.16800	0.33700	0.05210
O 5	–2	0.51400	0.02800	0.15190

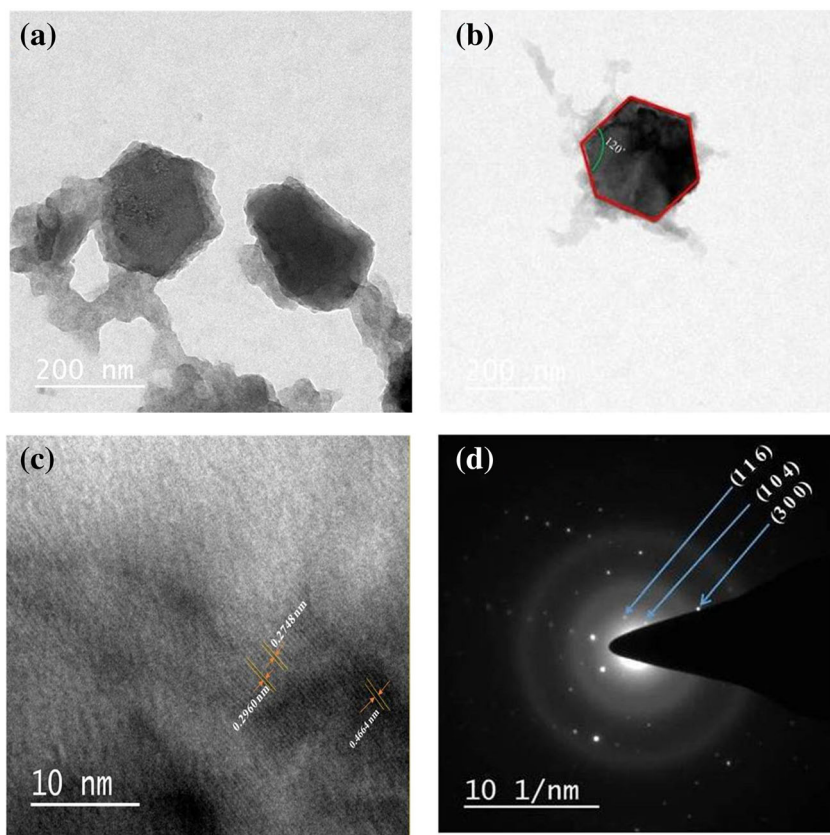
pattern are similar with XRD, which supports the hexagonal nature of the BHF ceramic.

Figure 5(a) shows that two different types of particle having perfect hexagonal shape and few of them have faceted grains separated by grain boundary. The calculated average grain size of the BHF ceramic is in the range  $0.3\text{--}1.0\text{ }\mu\text{m}$ . Grain size obtained by SEM analysis is larger than that of crystallite size calculated from XRD measurement. The higher grain size is explained due to its formation by combination of few particles. The EDX spectrum of the BHF ceramic corresponding to the SEM images shown in Fig. 5(b), confirms the presence of Ba, Fe, and O elements. The quantitative atomic percentage data of Ba, Fe, and O in BHF ceramic obtained from EDX data, are 2.94, 32.13, and 64.93 respectively. The observed atomic percentage data confirms the molecular formula as per their stoichiometric ratio. Figure 6(a) shows the clear grain boundaries with a comparable grain size of the BHF ceramic. The average roughness (Ra) and root mean



**Fig. 3** FTIR spectra of BHF ceramic sintered at  $1050\text{ }^\circ\text{C}$  for 12 h

**Fig. 4** (a) Bright field TEM image (b) Single hexagonal particle having characteristic hexagonal bond angle  $120^\circ$  (c) High-resolution TEM image with  $d$  spacing (d) Selected area diffraction (SAED) pattern of BHF ceramic



square ( $R_q$ ) data are obtained as 44.025 nm and 61.048 nm, respectively on scanned area  $11 \text{ mm} \times 11 \text{ mm}$ . The distribution of particles on the surface is also recorded by the three dimensional image shown in Fig. 6(b). The maximum peak-valley depth of two-dimensional structures is found to be 164.743 nm. Figure 6(c) reveals the histogram of grain size indicates the most of the grain are in size range of 300–600 nm, which substantiate with SEM results as mentioned earlier.

Figure 7(a) shows the magnetization curve of zero fields cooled (ZFC) and field cooled (FC) at the temperature of 5–300 K with the applied magnetic field 100 Oe. The magnetization on both ZFC and FC curves monotonically increases with decreasing temperature, and remains constant from 50 to

5 K. The FC and ZFC curve merged to each other, which clearly revealed that presence of only one magnetic phase and absence of spin-glass transition [24]. The M-H hysteresis loops recorded at  $\pm 2 \text{ T}$  for 5 and 300 K shown in Fig. 7(b). The remnant and saturation magnetization increases with decrease of temperature. The coercivity of material is relatively lower as reported earlier due to distribution of hexagonal particle is not homogeneous throughout the material [25]. Saturation magnetization are found to be 137.97 and 101.23 emu/g for 5 K and 300 K, respectively and these values are higher than the theoretical value due to high phase purity and well-defined crystallinity of  $\text{BaFe}_{12}\text{O}_{19}$  phase [26]. The squareness ratio ( $M_r/M_s$ ) is close to 0.6 for both temperatures, which indicates single domain crystal structure hard magnetic nature and

**Fig. 5** (a) SEM image and (b) EDX spectra corresponding to BHF ceramics sintered at  $1050^\circ\text{C}$  for 12 h

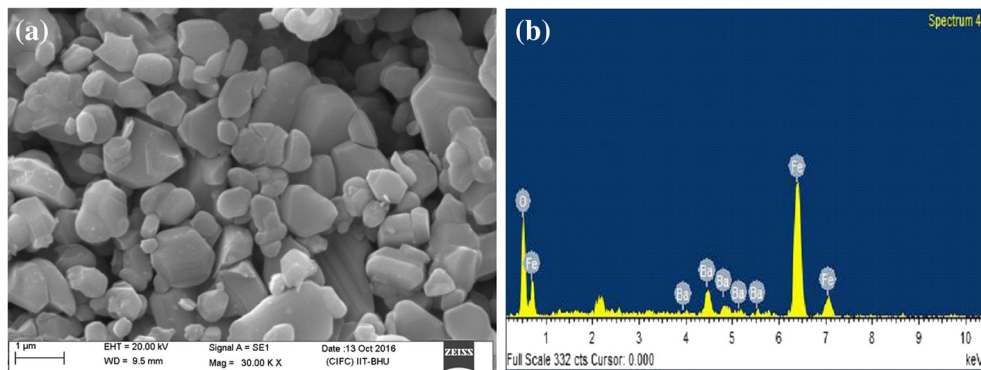
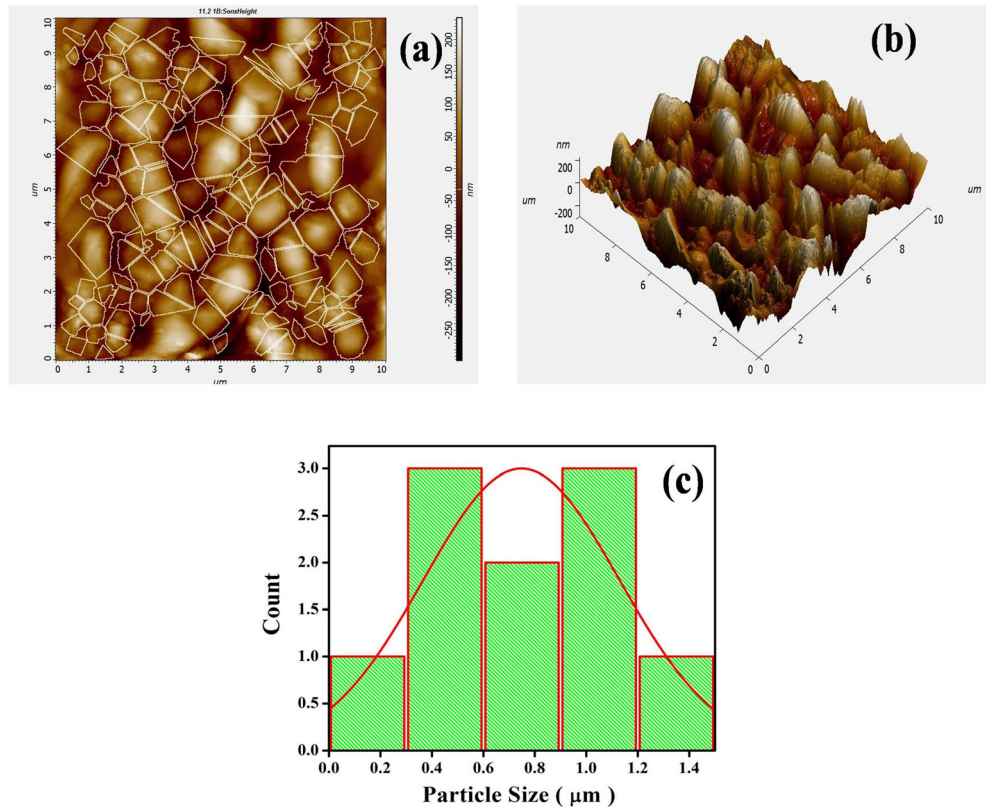


**Fig. 6** AFM images (a) 2D for grain boundaries (b) 3D for surface roughness and (c) Histogram graph for particle size distribution of BHF ceramic sintered at 1050 °C for 12 h



material is used as permanent magnet as well as magnetic recording devices. The magnetic parameters are mentioned in Table 3. The temperature dependence of inverse magnetic susceptibility for the BHF ceramic depicts in Fig. 8. The observed fitted plot follows the path of Curie–Weiss law, as represented in Eq. (2)

$$\chi = \frac{C}{T-\theta} \tag{2}$$

where  $\chi$ ,  $C$ ,  $\theta$  and  $T$  represents magnetic susceptibility, Curie constant and Curie-Weiss temperature and temperature, respectively. The experimental values of  $C$  and  $\theta$  are calculated and found to be  $285.0 \text{ emu g}^{-1} \text{ Oe}^{-1}$  and  $82 \text{ K}$ . The positive value of Curie–Weiss temperature ( $\theta$ ) emphasize that the BHF ceramics have ferromagnetic character [27].

The dielectric dispersion, as well as the formation of inter-barrier layer due to grain and grain boundary contribution in the BHF ceramic, can be understood by complex impedance spectroscopy (CIS) which provides the idea about an occurrence of the multi-polarization process and their relaxation conditions. The effective contribution due to grain, grain boundary and electrode interface can be determined by impedance plane plots. It differentiates grains, grain boundaries and electrode contributions by semicircular arcs. Semicircular arcs at low, middle and higher frequency side due to electrode, grain boundary and grain contributions, respectively. The complex impedance plots of the BHF ceramic sintered for

12 h at few selected temperature (303–483 K) is shown in Fig. 9(a) that reveals the presence of two semicircular arcs with different intercepts, which may be due to grain and grain boundary. The expanded view of impedance plots at higher frequency region is shown in the inset of Fig. 9(a), which suggests that the intercept on  $Z'$  axis possess through origin explain the existence of grain at the higher frequency region. The first and second semicircle arcs are represent grains resistance ( $R_g$ ) and grain boundary resistance ( $R_{gb}$ ), respectively. The Impedance of grains and grain boundaries is represented by the Eq. (3)

$$Z^* = \frac{1}{R_g^{-1} + i\omega C_g} + \frac{1}{R_{gb}^{-1} + i\omega C_{gb}} = Z' - iZ'' \tag{3}$$

Where

$$Z' = \frac{R_g}{1 + (\omega R_g C_g)^2} + \frac{R_{gb}}{1 + (\omega R_{gb} C_{gb})^2}$$

And

$$Z'' = R_g \left[ \frac{\omega R_g C_g}{1 + (\omega R_g C_g)^2} \right] + R_{gb} \left[ \frac{\omega R_{gb} C_{gb}}{1 + (\omega R_{gb} C_{gb})^2} \right]$$

The values of grain and grain boundary resistance are calculated and mentioned in Table 4. It is clear that resistance of

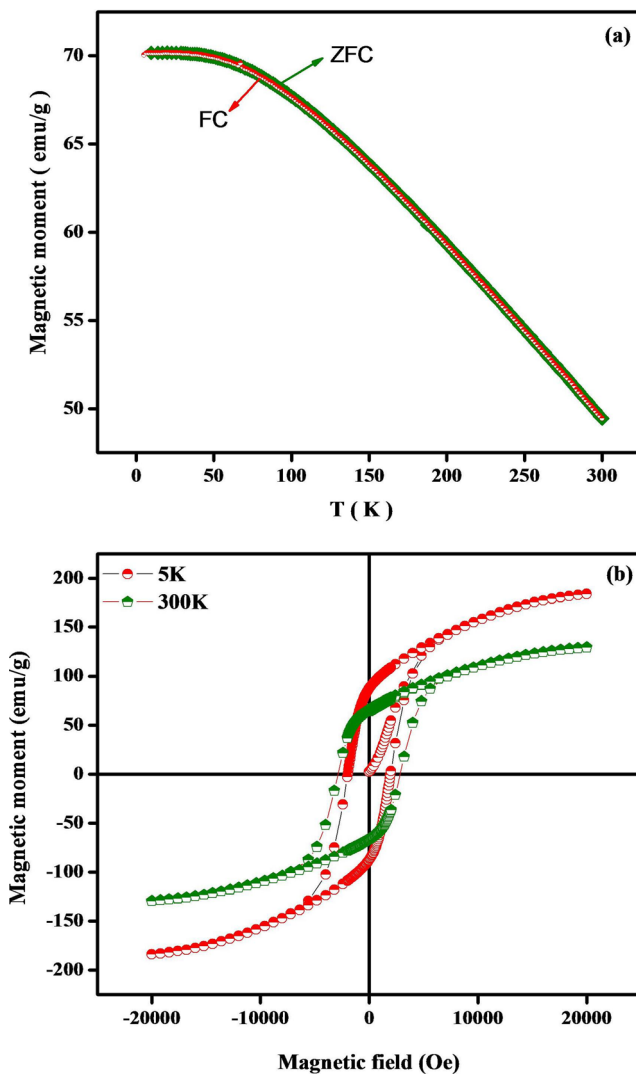


**Fig. 7** (a) Temperature-dependent ZFC and FC at  $H = 100$  Oe (b) M-H hysteresis at 5 and 300 K for the BHF ceramic

grains and grain boundaries decrease with increasing temperature. The suppression of grains arc occur at higher frequency region due to the higher value of grain boundaries resistance which is usually referred to IBLC mechanism that explains the conducting nature of grains with insulating grain boundaries [28]. The variation of imaginary impedance ( $Z''$ ) with frequency at few selected temperatures is shown in Fig. 9(b). The figure reveals that  $Z''$  decreases with increasing frequency and merge to each other in the higher frequency

**Table 3** Magnetic parameters of  $\text{BaFe}_{12}\text{O}_{19}$  ceramic at different temperature

T (K)	$M_s$ (emu/g)	$M_r$ (emu/g)	$M_r/M_s$	$H_c$ (A/m)
5	137.97	86.34	0.625	$1.48 \times 10^5$
300	101.23	64.21	0.634	$2.24 \times 10^5$

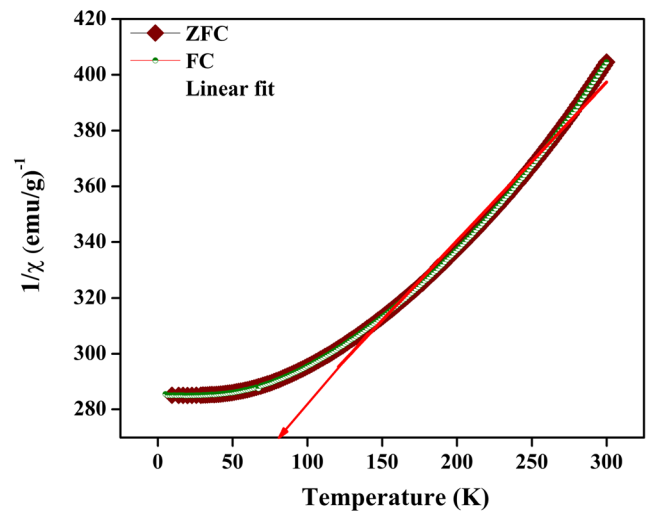
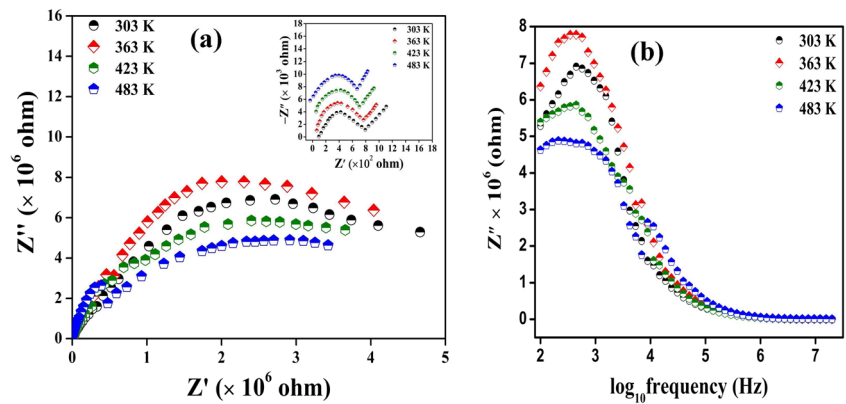


**Fig. 8** Plots of inverse magnetic susceptibility as a function of temperature recorded at  $\pm 2$  T and applied magnetic field  $H = 100$  Oe

region. The relaxation peaks observed at lower frequency regions and suppression of peaks at higher frequency explain temperature-dependent thermally assisted ionic phenomenon of the BHF ceramic.

Frequency dependent dielectric constants ( $\epsilon'$ ) at a few selected temperatures are shown in Fig. 10(a). The dielectric constant below 10 kHz increases with decrease in frequency and remains constant from 10 kHz to 20 MHz. The decreasing behavior of dielectric constant with frequency is explained by Maxwell–Wagner phenomena, which arises due to inhomogeneity in conductivity of grains and grain boundaries at the interface [29, 30]. The value of dielectric constant is found in order of  $\sim 10^3$  at 483 K and 100 Hz. The logarithmic scale of dielectric constant at higher frequency region is shown in the inset of Fig. 10(a) which shows the clear vision of dielectric constant at higher frequencies. Figure 10(b) shows variation in dielectric loss ( $\tan \delta$ ) as a function of frequency ( $10^2$ – $10^7$  Hz) at few selected temperatures. The values of  $\tan \delta$  are found to be 19, 53, 72, and 111 at temperature 303 K, 383 K, 423 K, 483 K and 100 Hz respectively. The values of  $\tan \delta$  are almost independent in the higher frequency range ( $10^5$ – $10^7$  Hz) and show low value of  $\tan \delta$  (0.9) as indicated in the inset. Figure 11 indicates the variation of dielectric constant ( $\epsilon'$ ) and dielectric loss ( $\tan \delta$ ) with the temperature at few selected frequencies. Relaxation peaks are observed at 100 Hz, 1 kHz and 10 kHz at 400 K, which shift towards high temperature range so the Curie temperature also increases with frequency [31]. Figure 11(b) shows that dielectric loss ( $\tan \delta$ ) of the BHF ceramic increases with increase in temperature. A rapid increase in  $\tan \delta$  at higher temperature is due to the exponential enhancement in conductivity with temperature, which arises due to oxygen vacancy present in BHF ceramics during the sintering process [32–35]. The dependence of imaginary dielectric constant ( $Z''$ ) on frequency at few selected temperature for the BHF ceramic is shown in Fig. 12. It

**Fig. 9** (a) complex Impedance plane plots ( $Z'$  vs  $Z''$ ) at few selected temperature (b) Plots of imaginary impedance ( $Z''$ ) with frequency at few selected temperatures for BHF ceramic sintered at 1050 °C for 12 h



exhibits higher values of ( $\epsilon''$ ) at the lower frequency and higher temperature and rapidly decreases with increasing frequency. The dielectric constant decreases with increasing frequency may be Maxwell interfacial polarization. The constant value of  $\epsilon''$  in the higher frequency region occurs due to periodic reversal of the field so that no charge accumulation at the interface. Impedance studies also clarify lower and the higher resistance value of grain and insulating grain boundary with different conductivity, which causes inhomogeneity in the BHF ceramic. The imaginary part of dielectric constant ( $\epsilon''$ ) as a function of frequency related with Maxwell–Wagner expressed as the following Eq. (4)

$$\epsilon'' = \frac{1}{\omega C_0 (R_{gb} + R_g)} \frac{1 - \omega^2 \tau_{gb} \tau_g + \omega^2 \tau (\tau_{gb} + \tau_g)}{1 + \omega^2 \tau^2} \quad (4)$$

Where,

$$\tau_g = C_g R_g \text{ and } \tau_{gb} = C_{gb} R_{gb}$$

$$\tau = \frac{\tau_{gb} R_g + \tau_g R_{gb}}{R_{gb} + R_g}, C_0 = \epsilon_0 \frac{1}{A}$$

where subscript g and gb represents grains and grain boundaries, respectively,  $\tau$  is the relaxation time,  $\omega$  is the angular frequency, l and A are thickness and area of the cylindrical pellets. The Maxwell -Wagner relaxation is clearly shown in inset of the figure at higher frequency region [36].

**Table 4** Calculated values of resistance (R) and capacitance (C) of grain and grain boundary at few selected temperature for barium hexaferrite (BaFe12O19) ceramic

Temperature(K)	R <sub>g</sub> (ohm)	R <sub>gb</sub> (ohm)	C <sub>g</sub> (pF)	C <sub>gb</sub> (pF)
303 K	849.25	4,796,430	0.120	0.581
363 K	790.45	4,201,259	0.166	0.849
423 K	728.99	3,748,787	0.230	1.223
483 K	638.69	3,467,455	0.337	1.695

The conductivity ( $\sigma$ ) associated with AC and DC contribution on frequency is expressed by the equation.

$$\sigma = \sigma_{dc} + \sigma_{ac} = \sigma_{dc} + A\omega^s \quad (5)$$

At higher frequencies, conductivity obeys Jonscher’s law  $\sigma(\omega) \propto \omega^s$  where  $s < 1$  [37]. Where A is the pre-exponential factor,  $\omega$  is angular frequency,  $\sigma_{dc}$  and  $\sigma_{ac}$  are the frequency independent conductivity (DC) and frequency dependent conductivity (AC), and s is the dimensionless frequency exponent

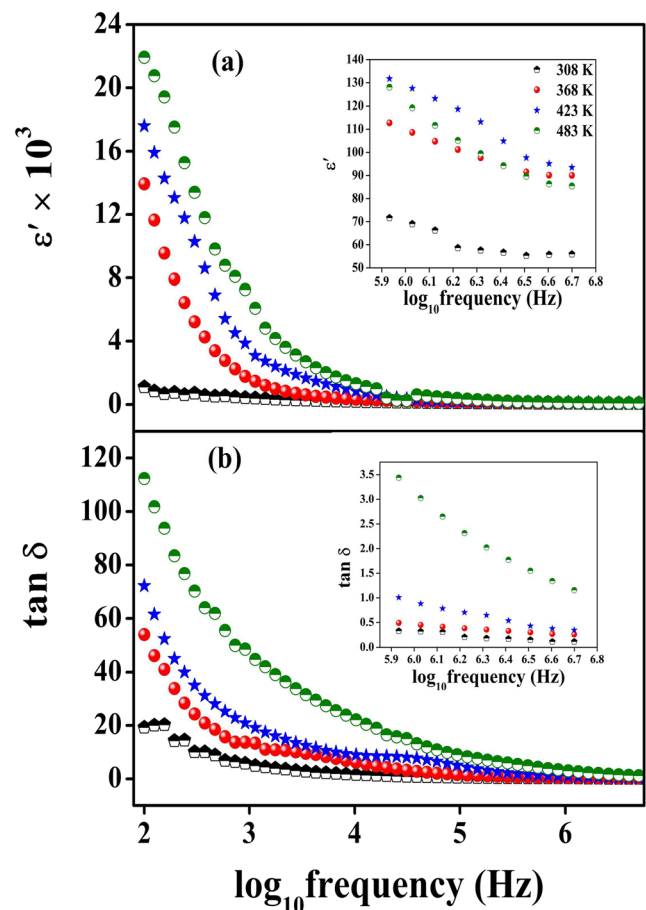


**Fig. 10** (a) dielectric constant ( $\epsilon'$ ) and (b) dielectric loss ( $\tan \delta$ ) as a function of frequency at few selected temperatures

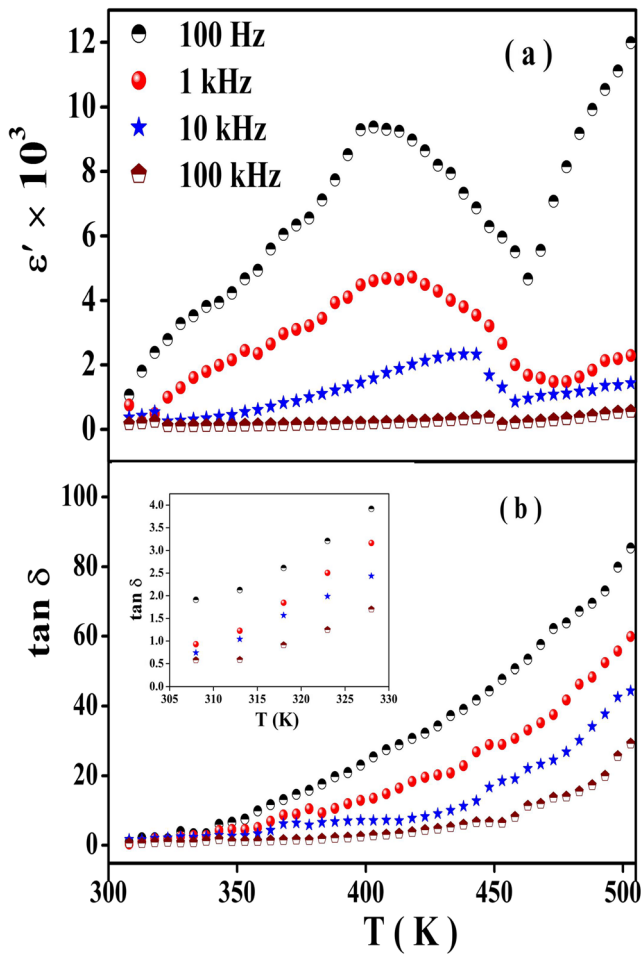


Fig. 11 Temperature dependent (a) dielectric constant ( $\epsilon'$ ) and (b) dielectric loss ( $\tan \delta$ ) at few selected frequencies

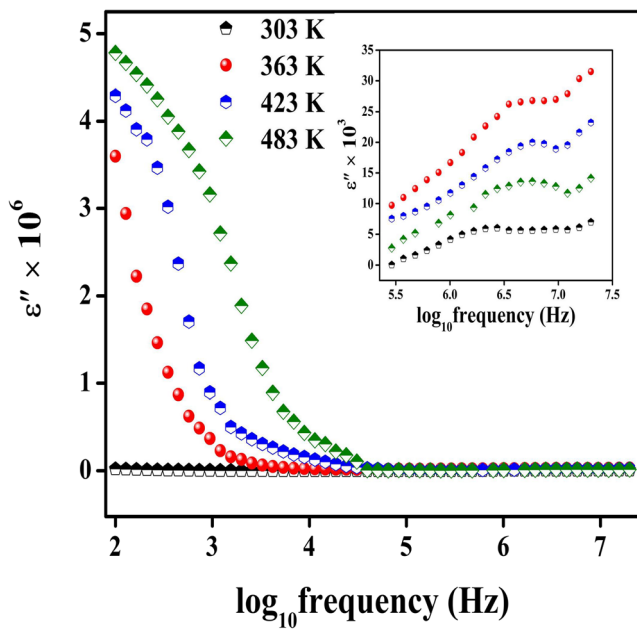


Fig. 12 Plots of Imaginary dielectric constant ( $\epsilon''$ ) vs frequency at few selected temperature sintered at 1050 °C for 12 h

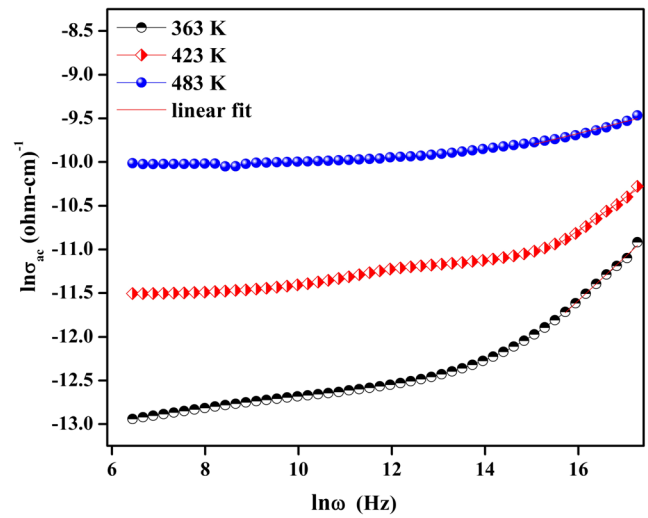


Fig. 13 Frequency dependent AC conductivity at few selected temperatures

parameters. Figure 13 shows frequency dependence of AC conductivity at few selected temperatures. The critical frequency ( $\omega_c$ ) is found to be 15.06 Hz. The value of frequency exponent parameter ( $s$ ) obtained from the slope of the plot ( $\ln \sigma$  vs.  $\ln \omega$ ) for BHF ceramic are found to be 0.50, 0.37, and 0.13 at the temperature 363, 423 and 483 K respectively. Such frequency dependent conductivity explained regarding Correlated Barrier Hopping (CBH) model, given by Elliot for crystalline oxide materials [38].

Figure 14 shows the temperature - dependent conductivity at different frequencies. It reveals from figure that conductivity increases with increase in temperature, which suggests that at lower temperature region DC conductivity predominant over AC conductivity because  $\sigma_{ac}$  considerably depends on the frequency. As temperature increases dielectric relaxation takes place, which reduces the frequency dependence of AC

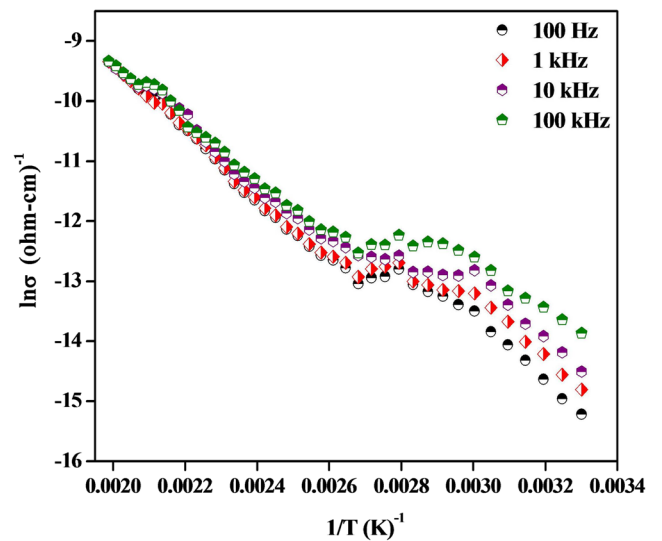


Fig. 14 Plots of conductivity with inverse of temperature at few selected frequencies



conductivity. Therefore, conductivity mainly depends on temperature. According to Arrhenius law, temperature dependent conductivity ( $\sigma$ ) expressed by the following equation

$$\sigma = \sigma_0 e^{-E_a/kT} \quad (6)$$

where  $E_a$  is the activation energy for ionic conduction,  $\sigma_0$  pre-exponential factor  $k$  is the Boltzmann constant, and  $T$  is the absolute temperature. Two different slopes are observed corresponds to lower and higher temperatures. The activation energy in the high-temperature region is found to be 0.46 eV in all measured frequencies. At higher temperature, AC and DC remains same due to curves are merge to each and onset of intrinsic conductivity take place [39]. At lower temperature region the activation energy ( $E_a$ ) of BHF ceramic are found to be 0.50, 0.48, 0.45 and 0.29 eV at 100 Hz, 1 kHz, 10 kHz, and 100 kHz respectively. It is seen that  $E_a$  decrease with increasing frequency, which may be due to enhancement of electronic jumps between two sites on increasing of applied frequency. The lower value of activation energy observed at the higher frequency due to hopping charge mechanism between  $Fe^{+3}$  and  $Fe^{+2}$  ions which increase conductivity.

## 4 Conclusions

Hexagonal BHF ceramic was synthesized by the chemical method sintered at 1050 °C for 12 h. XRD confirmed the single phase without any signature of the secondary phase. The structure, chemical composition, and microstructure were examined using XRD, EDX and SEM analysis. Rietveld refinement analysis confirms hexagonal structure of BHF ceramic with space group  $P6_3/mmc$  (194) and lattice parameter  $a = b = 5.895 \text{ \AA}$  and  $c = 23.199 \text{ \AA}$ . This material exhibits excellent dielectric and magnetic properties. The value of dielectric constant was found to be very high ( $\epsilon' \sim 22 \times 10^3$ ) at 100 Hz, and 483 K. Magnetic hysteresis loop shows the ferromagnetic to the paramagnetic behavior of material on increasing temperature. Larger the value of squareness ( $M_r/M_s$ ) ratio obtained from hysteresis loop of this ceramic justifies its suitability in various applications such as high magnetic recording media and the permanent magnet. The temperature dependent AC conductivity and frequency exponent parameters ( $s$ ) were interpreted in the terms of Correlated Barrier Hopping (CBH) model.

**Acknowledgements** Authors would like to thanks, Prof. Rajeev Prakash, In-charge of Central Instrument Facility Center (CIFIC) IIT (BHU) for providing SEM, TEM and MPMS facilities.

## References

1. Ü. Özgür, Y. Alivov, H. Morkoc, *J. Mater. Sci. Mater. Electron.* **20**, 789 (2009)
2. R.C. Pullar, *Prog. Mater. Sci.* **57**(7), 1191–1334 (2012)
3. Ü. Özgür, Y. Alivov, *J. Mater. Sci. Mater. Electron.* **20**, 911 (2009)
4. S. Singhal, T. Namgyal, J. Singh, K. Chandra, S. Bansal, *Ceram. Int.* **37**(6), 1833–1837 (2011)
5. W. Onreabroy, K. Papato, G. Rujijanagul, K. Pengpat, T. Tunkasiri, *Ceram. Int.* **38**, 415 (2012)
6. X. Zhang, Y. Duan, H. Guan, S. Liu, B. Wen, *J. Magn. Magn. Mater.* **311**(2), 507–511 (2007)
7. H. Cho, S. Kim, *IEEE Trans. Magn.* **35**, 3151 (1999)
8. C. Li, B. Wang, J. Wang, *J. Magn. Magn. Mater.* **324**, 1305 (2012)
9. V.K. Sankaranarayanan, Q.A. Pankhurst, D.P.E. Dickson, C.E. Johnson, *J. Magn. Magn. Mater.* **120**(1–3), 73–75 (1993)
10. M.-L. Wang, Z.-W. Shih, C.-H. Lin, *J. Cryst. Growth* **130**(1–2), 153–161 (1993)
11. P. Xu, X. Han, H. Zhao, Z. Liang, J. Wang, *Mater. Lett.* **62**(8–9), 1305–1308 (2008)
12. M. El-Hilo, H. Pfeiffer, K. O'Grady, W. Schuppel, E. Sinn, P. Gornert, M. Rosler, D.P.E. Dickson, R.W. Chantrell, *J. Magn. Magn. Mater.* **129**(2–3), 339–347 (1994)
13. C. Sudakar, G.N. Subbanna, T.R.N. Kutty, *J. Magn. Magn. Mater.* **263**(3), 253–268 (2003)
14. K.V.P.M. Shafi, A. Gedanken, *NanoStruct. Mater.* **12**, 29 (1999)
15. V.V. Pankov, M. Pernet, P. Germi, P. Mollard, *J. Magn. Magn. Mater.* **120**(1–3), 69–72 (1993)
16. O. Carp, R. Barjega, E. Segal, M. Brezeanu, *Thermochim. Acta* **318**, 57 (1998)
17. P. Sharma, R.A. Rocha, S.N. de Medeiros, A. Paesano Jr., *J. Alloys Compd.* **443**(1–2), 37–42 (2007)
18. K.F. Wang, j.-M. Liu, Z.F. Ren, *Adv. Phys.* **58**(4), 321–448 (2009)
19. H. Pfeiffer, R.W. Chantrell, P. Gornert, W. Schuppel, E. Sinn, M. Rosler, *J. Magn. Magn. Mater.* **125**(3), 373–376 (1993)
20. M.M. Rashad, M. Radwan, M.M. Hessien, *J. Alloys Compd.* **453**(1–2), 304–308 (2008)
21. K.K. Mallick, P. Shepherd, R.J. Green, *J. Eur. Ceram. Soc.* **27**, 2024 (2007)
22. Y. Maswadeh, S.H. Mahmood, A. Awadallah, A.N. Aloqaily, *Mater. Sci. Eng.* **92**, 012019 (2015)
23. G.R. Gordani, A. Ghasemi, A. Saidi, *Ceram. Int.* **40**(3), 4945–4952 (2014)
24. B. Martinez, X. Obradors, L. Balcells, A. Rouanet, C. Monty, *Phys. Rev. Lett.* **80**(1), 181–184 (1998)
25. O. Kubo, T. Ido, H. Yokoyama, Y. Koike, *Appl. Phys.* **57**(8), 4280–4282 (1985)
26. B.T. Shhirk, W.R. Buessem, *J. Appl. Phys.* **40**(3), 1294–1296 (1969)
27. M.T. Azcondo, J.R. de Paz, K. Boulahya, C. Ritter, F. Garcia-Alvarado, U. Amador, *Dalton Trans.* **44**(8), 3801–3810 (2015)
28. S. Sharma, S.S. Yadava, M.M. Singh, K.D. Mandal, *J. Adv. Dielect.* **4**(04), 1450030 (2014)
29. M. George, S.S. Nair, K.A. Malini, P.A. Joy, M.R. Anantharaman, *Appl. Phys.* **40**, 1593 (2007)
30. C.G. Koops, *Phys. Rev.* **83**, 121 (1951)
31. C. Mu, H. Zhang, Y. He, J. Shen, P. Liu, *J. Phys. D: Appl. Phys.* **42**(17), 175410 (2009)
32. S.S. Yadava, L. Singh, S. Sharma, K.D. Mandal, N.B. Singh, *RSC Adv.* **6**(72), 68247–68253 (2016)
33. A. Khare, S.S. Yadava, K.D. Mandal, N.K. Mukhopadhyay, *Microelectron. Eng.* **164**, 1–6 (2016)
34. L. Singh, S.S. Yadava, B.C. Sin, U.S. Rai, K.D. Mandal, Y. Lee, *J. Electron. Mater.* **45**(6), 2662–2672 (2016)

35. P. Gautam, S.S. Yadava, A. Khare, K.D. Mandal, *Ceram. Int.* **43**(3), 3133–3139 (2017)
36. T. Wang, J. Hu, H. Yang, L. Jin, X. Wei, C. Li, F. Yan, Y. Lin, *J. Appl. Phys.* **121** (2017)
37. J.C. Dyre, T.B. Schroder, *Am. Phys. Soc.* **72**, 873 (2000)
38. S.R. Elliott, *Solid State Ionics* **70**, 27 (1994)
39. N.V. Prasad, G. Prasad, T. Bhimasankaram, S.V. Suryanarayana, G.S. Kumar, *Synthesis. Bull. Mater. Sci.* **24**(5), 487–495 (2001)